Near-field observation of light propagation in nanocoax waveguides

Juan M. Merlo,* Fan Ye, Binod Rizal, Michael J. Burns, and Michael J. Naughton

Department of Physics, Boston College, Chestnut Hill, Massachusetts 02467, USA
*juan.merlo@bc.edu

Abstract: We report the observation of propagating modes of visible and near infrared light in nanoscale coaxial (metal-dielectric-metal) structures, using near-field scanning optical microscopy. Together with numerical calculations, we show that the propagated modes have different nature depending on the excitation wavelength, *i.e.*, plasmonic TE_{11} and TE_{21} modes in the near infrared and photonic TE_{31}, TE_{41} and TM_{11} modes in the visible. Far field transmission out of the nanocoaxes is dominated by the superposition of Fabry-Perot cavity modes resonating in the structures, consistent with theory. Such coaxial optical waveguides may be useful for future nanoscale photonic systems.

OCIS codes: (180.0180) Microscopy; (240.6680) Surface plasmons; (230.7370) Waveguides.

References and links

1. V. J. Sorger, Z. Ye, R. F. Oulton, Y. Wang, G. Bartal, X. Yin, and X. Zhang, "Experimental demonstration of low-loss optical waveguiding at deep sub-wavelength scales," Nat. Commun. **2**, 331 (2011).
2. J. H. Park, C. Park, H. S. Yu, J. Park, S. Han, J. Shin, S. H. Ko, K. T. Nam, Y. H. Cho, and Y. K. Park, "Subwavelength light focusing using random nanoparticles," Nat. Photonics **7**(6), 454–458 (2013).
3. D. Pozar, *Microwave Engineering* (John Wiley and Sons, 2005).
4. W. Thomson, "On the theory of the electric telegraph," Proc. R. Soc. Lond. **7**(0), 382–399 (1854).
5. F. I. Baida, A. Belkhir, D. Van Labeke, and O. Lamrous, "Subwavelength metallic coaxial waveguides in the optical range: Role of the plasmonic modes," Phys. Rev. B **74**(20), 205419 (2006).
6. F. I. Baida, D. van Labeke, G. Granet, A. Moreau, and A. Belkhir, "Origin of the super-enhanced light transmission through a 2-D metallic annular aperture array: a study of photonic bands," Appl. Phys. B **79**(1), 1–8 (2004).
7. R. de Waele, S. P. Burgos, H. A. Atwater, and A. Polman, "Negative refractive index in coaxial plasmon waveguides," Opt. Express **18**(12), 12770–12778 (2010).
8. A. A. E. Saleh and J. A. Dionne, "Waveguides with a silver lining: Low threshold gain and giant modal gain in active cylindrical and coaxial plasmonic devices," Phys. Rev. B **85**(4), 045407 (2012).
9. Y. Poujet, M. Roussey, J. Salvi, F. I. Baida, D. Van Labeke, A. Perentes, C. Santschi, and P. Hoffmann, "Super-transmission of light through subwavelength annular aperture arrays in metallic films: Spectral analysis and near-field optical images in the visible range," Phot. Nano. Fund. Appl. **4**(1), 47–53 (2006).
10. J. Rybczynski, J. Kempa, A. Herczynski, Y. Wang, M. J. Naughton, Z. F. Ren, A. P. Huang, D. Cai, and M. Giersig, "Subwavelength waveguide for visible light," Appl. Phys. Lett. **90**(2), 021104 (2007).
11. Y. Peng, X. Wang, and K. Kempa, "TEM-like optical mode of a coaxial nanowaveguide," Opt. Express **16**(3), 1758–1763 (2008).
12. K. Kempa, X. Wang, Z. F. Ren, and M. J. Naughton, "Discretely guided electromagnetic effective medium," Appl. Phys. Lett. **92**(4), 043114 (2008).
13. M. Khajavikhan, A. Simic, M. Katz, J. H. Lee, B. Slutsky, A. Mizrahi, V. Lomakin, and Y. Fainman, "Thresholdless nanoscale coaxial lasers," Nature **482**(7384), 204–207 (2012).
14. Z. G. Chen, J. Zou, G. Q. Lu, G. Liu, F. Li, and H. M. Cheng, "ZnS nanowires and their coaxial lateral nanowire heterostructures with BN," Appl. Phys. Lett. **90**(10), 103117 (2007).
15. C. H. Hsieh, M. T. Chang, Y. J. Chien, L. J. Chou, L. J. Chen, and C. D. Chen, "Coaxial Metal-Oxide-Semiconductor (MOS) Au/Ga2O3/GaN Nanowires," Nano Lett. **8**(10), 3288–3292 (2008).
16. B. Di Bartolo, J. Collins, and L. Silvestri, *Nano-Optics for Enhancing Light-Matter Interactions on a Molecular Scale* (Springer, 2013), Ch. 18.
17. M. J. Naughton, K. Kempa, Z. F. Ren, Y. Gao, J. Rybczynski, N. Argenti, W. Gao, Y. Wang, Y. Peng, J. R. Naughton, G. McMahon, T. Paudel, Y. C. Lan, M. J. Burns, A. Shepard, M. Clary, C. Ballif, F.-J. Haug, T. Söderström, O. Cubero, and C. Eminian, "Efficient nanocoax-based solar cells," Phys. Status Solidi RRL **4**(7), 181–183 (2010).

#210870 - $15.00 USD Received 25 Apr 2014; revised 19 May 2014; accepted 22 May 2014; published 2 Jun 2014

18. T. Paudel, J. Rybczynski, Y. T. Gao, Y. C. Lan, Y. Peng, K. Kempa, M. J. Naughton, and Z. F. Ren, "Nanocoax solar cells based on aligned multiwalled carbon nanotube arrays," Phys. Status Solidi A **208**(4), 924–927 (2011).
19. H. Zhao, B. Rizal, G. McMahon, H. Wang, P. Dhakal, T. Kirkpatrick, Z. Ren, T. C. Chiles, M. J. Naughton, and D. Cai, "Ultrasensitive chemical detection using a nanocoax sensor," ACS Nano **6**(4), 3171–3178 (2012).
20. B. Rizal, M. M. Archibald, T. Connolly, S. Shepard, M. J. Burns, T. C. Chiles, and M. J. Naughton, "Nanocoax-based electrochemical sensor," Anal. Chem. **85**(21), 10040–10044 (2013).
21. J. M. Merlo, J. F. Aguilar, H. Gonzalez-Hernandez, and N. Caballero, "Properties of the near field interactions produced by spherical nanoparticles," Proc. SPIE **8011**, 801141 (2011).
22. F. Ye, M. J. Burns, and M. J. Naughton, "Plasmonic halos--Optical surface plasmon drumhead modes," Nano Lett. **13**(2), 519–523 (2013).
23. J. Lin, J. P. Mueller, Q. Wang, G. Yuan, N. Antoniou, X. C. Yuan, and F. Capasso, "Polarization-controlled tunable directional coupling of surface plasmon polaritons," Science **340**(6130), 331–334 (2013).
24. D. Courjon, *Near Field Microscopy and Near Field Optics* (Imperial College, 2003).
25. L. Novotny and B. Hecht, *Principles of Nano-Optics* (Cambridge University, 2006).
26. P. B. Johnson and R. W. Christy, "Optical constants of noble metals," Phys. Rev. B **6**(12), 4370–4379 (1972).
27. http://refractiveindex.info/?group=CRYSTALS&material=Al2O3
28. M. Bednorz, M. Urbańczyk, T. Pustelny, A. Piotrowska, E. Papis, Z. Sidor, and E. Kamińska, "Application of SU8 polymer in waveguide interferometer ammonia sensor," Mol. Quant. Acoust. **27**, 31–40 (2006).
29. R. A. Kirkman and M. Kline, "The transverse electric modes in coaxial cavities," Proc. I.R.E. **34**, 14 – 17 (1946).
30. O. Kozina, I. Nefedov, L. Melnikov, and A. Karilainen, "Plasmonic coaxial waveguides with complex shapes of cross-sections," Materials **4**(1), 104–116 (2011).
31. R. de Waele, S. P. Burgos, A. Polman, and H. A. Atwater, "Plasmon dispersion in coaxial waveguides from single-cavity optical transmission measurements," Nano Lett. **9**(8), 2832–2837 (2009).

1. Introduction

Modern fabrication technologies allow the miniaturization of optical components to subwavelength size scales, opening new frontiers in the nanoscale manipulation of light [1, 2]. Having been studied and developed for more than a century in radio technology [3], the coaxial waveguide, whose origins can be traced to Thomson (Kelvin) [4], can be considered one of the more promising architectures for subwavelength optical utilization. Over the last decade, several theoretical works have studied the properties of light propagating in subwavelength coaxial waveguides [5–8], providing a good understanding of the propagation properties. An early experimental attempt of near-field observation of the radiation pattern produced by a coaxial structure was made by Poujet *et al.* [9], but the image clarity was low relative to more recent microscopy capabilities. The first observation of the propagation of light through nanoscale coaxial waveguides and into the far field was by Rybczynski *et al*. [10], who built and studied such subwavelength coaxial waveguides, proposing propagation distances as long as 50 μm in the absence of a cut-off wavelength. A theoretical analysis of coaxial waveguide behavior was provided by Peng *et al.* [11], who showed that a subwavelength coaxial waveguide can support a TEM-like (transverse electromagnetic) plasmonic mode. This mode can also be propagated without cut-off, when the excitation frequency is much lower than the plasma frequency of the metal used in the electrodes, resulting in a conceptual extension of the radio frequency (RF) coaxial waveguide to the visible. Later, Kempa *et al.* [12] calculated the transmission efficiency of subwavelength coaxial arrays and concluded that it can reach 90%, when the coupled optical field is via a TM_{00} mode, which at long wavelengths reduces to the TEM mode. Recently, deep subwavelength coaxial structures have become important because new applications appeared, such as high efficiency optical trapping [8] and high temperature laser cavities [13]. Relatedly, nanoscale coaxial structures have been fabricated in ordered arrays, using methodologies developed during the last decade, which heretofore have resulted in low reproducibility and low scale fabrication [14, 15]. In this sense, our group has developed a large scale (~10 cm^2) fabrication process of so called *nanocoax* arrays [16], with high site density (10^6 per mm^2), high reproducibility and good optical performance. Such nanocoax arrays have recently found applications in fields as different as high efficiency photovoltaics [17, 18] and ultrasensitive chemical [19] and electrochemical [20] sensing.

#210870 - $15.00 USD Received 25 Apr 2014; revised 19 May 2014; accepted 22 May 2014; published 2 Jun 2014

The most commonly-employed tool for observation of electromagnetic interactions in the subwavelength regimen is the near-field scanning optical microscope (NSOM) [21–23]. In brief, NSOM measures both near-field intensity and surface topography simultaneously by scanning an optical probe in close proximity (<50 nm) to a sample surface. The optical probe usually has a small aperture at the extreme end (~100 nm diameter), which determines the imaging spatial resolution [24]. The advantage of near-field imaging is the high correlation between optical intensity and topography, without diffraction effects as those present in conventional optical systems, *i.e.* NSOM is a non-diffraction limited imaging system [25].

2. Experimental methods

Nanocoax arrays were prepared following the technique reported by Rizal *et al*. [16], where SU-8 polymer pillars of 2 μm height were nanoimprinted in a hexagonal close-packed lattice (1.3 μm pitch) and coated with 125 nm of Au, creating the coax core. The coax annulus dielectric was a layer of 250 nm thick Al_2O_3, with a second 125 nm Au coating comprising the shield. The full array area was then spin coated with SU-8, exposed to UV light and baked. This latter coating was applied in order to structurally stabilize the array, filling the space between coaxes. Next, the sample was mechanically polished using a suspension of 50 nm alumina particles in a vibratory polisher until the outer electrode was exposed. Finally, wet etching process using Transetch-N solution was used to generate a cavity in the Al_2O_3 about 1 μm in depth, *i.e.* in the inter-electrode space. Note that the array was supported by a transparent glass substrate, allowing the coupling of light from the back side. Figure 1(a) shows a scanning electron microscope (SEM) image of a region of the sample (tilted 30°), where a transverse cut was made by focused ion beam milling, in order to expose the component layers of the structures. The inset is a colorized representation of one exposed nanocoax. Green regions correspond to SU-8, red to Al_2O_3 and yellow to Au.

We conducted measurements using an NSOM (Nanonics Multiview 4000) in collection mode with a ~100 nm aperture probe, with force detection based on a quartz tuning fork sensor. The sample-probe distance was about 20 nm in constant distance mode [24]. The total scanned area was 10 × 10 μm^2 with resolution of 400 × 400 points (25 nm/point). The sample was illuminated from the back with linearly polarized laser sources at near-infrared and visible wavelengths. The incident beam was focused by a 10 × microscope objective resulting in a spot size of 500 μm. Thus, the illuminated area was much larger than the size of an individual nanocoax. Figure 1(b) depicts a schematic of the experimental setup.

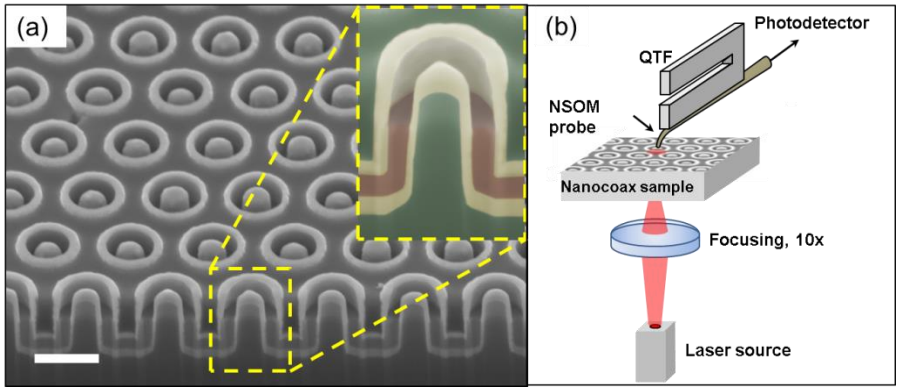

Fig. 1. (a) SEM image of the nanocoax array. The distance between centers is ~1.3 μm in a hexagonal close-packed lattice. Scale bar: 1 μm. The inset shows a magnification of one coax, where green corresponds to SU-8, red to Al_2O_3 and yellow to Au. (b) Schematic experimental setup of the NSOM system. The image scale is not the real. QTF = quartz tuning fork.

#210870 - $15.00 USD Received 25 Apr 2014; revised 19 May 2014; accepted 22 May 2014; published 2 Jun 2014

3. Results

Figure 2(a)-2(d) shows NSOM images corresponding to 850, 660, 532 and 473 nm illumination, respectively. The measured intensities are presented using the respective colors of the wavelengths employed in order to enable accurate visual recognition, with the exception of the 850 nm data, where an arbitrary color was chosen. As the dielectric response of the medium in the coax annulus (air or Al_2O_3) is linear, the output color is the same as the input. The polarization of the incident *E*-field is along the vertical direction. The circles represent the inner and outer diameters of the dielectric in the coax annulus, accordingly with topographic images. In Fig. 2(a) (850 nm wavelength), it is possible to observe two intensity lobes that follow the shape of the inner electrode, radiating parallel to the polarization direction of the excitation field. On the other hand, in the images where the excitation field had wavelengths in the visible range (Fig. 2(b)-2(d)), it is clear that the propagated field is confined to the inter-electrode space and appears as two intensity lobes oriented perpendicular to the polarization of the excitation field. In order to demonstrate the last statement, we show in Fig. 2(e) three-dimensional representations of the topography of a single nanocoax acquired by atomic force microscopy (AFM) and the near-field intensity when the wavelength was 532 nm (from Fig. 2(c)). As before, the circles represent the inner and outer diameters of the dielectric in the coax annulus and the vertical lines are visual guides to identify the positions of such boundaries.

We have simulated the propagation properties of this nanocoax structure, calculating the magnitude of the electric field using a three-dimensional model based on the finite element method (COMSOL 4.3b). The geometrical parameters are those of the fabricated structure and the refractive indices were taken from the literature for Au [26] and Al_2O_3 [27]. The developed SU-8 resist has weak dispersion in the visible range, and its refractive index was considered as constant and equal to 1.52 [28]. The excitation sources were monochromatic waves, linearly polarized and illuminating the sample from the back side, as in the experiment. Figure 2(f)-2(i) shows the simulated magnitude of the optical intensity ($\sim E^2$) averaged over one temporal period. The image colors were set as in the experimental results. Note that the calculated intensity for the 850 nm wavelength (Fig. 2(f)) shows radiation in the same direction as the polarization of the excitation field and following the shape of the inner electrode with intensity decay in the radial direction. When the excitation wavelength was in the visible range, Fig. 2(g)-2(i), on the other hand, the field is localized in the inter-electrode space (coax annulus), and can be visualized as rounded arc shapes.

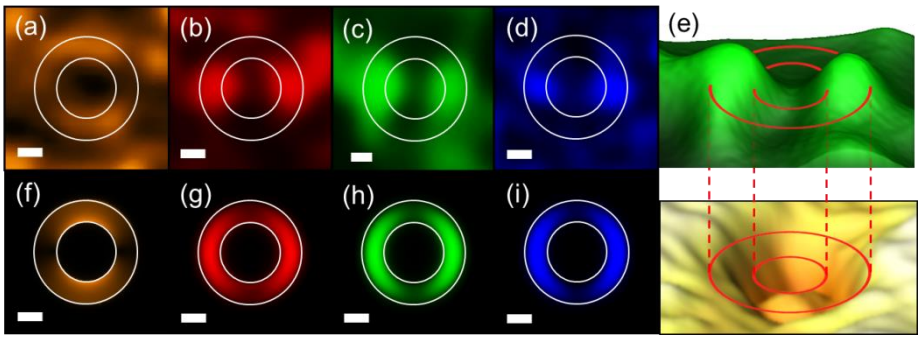

Fig. 2. NSOM-measured (a - d) and calculated (f - i) images of the propagated modes in the nanocoax structure. The wavelengths were 850 nm (a, f), 660 nm (b, g), 532 nm (c, h) and 473 nm (d, i). In all cases, the polarization is in the vertical direction, the scale bars represent 200 nm and circles represent the inner and outer radii of the coax annuli. (e) Three-dimensional representation of the nanocoax topography (lower, via AFM) and the corresponding near-field intensity (upper) for 532 nm wavelength.

#210870 - $15.00 USD Received 25 Apr 2014; revised 19 May 2014; accepted 22 May 2014; published 2 Jun 2014

The simulations are consistent with our experimental results but there are some differences with the experimental data, *i.e.*, in the experimental images where the excitation is in the visible wavelengths (and the field is located at the inter-electrode space), the intensity lobes appear as somewhat circular zones, as opposed to the rounded arc shape in the simulations. We consider this difference to be an artifact of the finite probe aperture size. Such an artifact can be explained as follows: in the fabrication process of the NSOM probe, where in order to create the optical aperture, the probe is coated with metal, in our case ~100 nm Au, resulting in a probe with a total cross section of about 300 nm diameter. This finite cross-section affects the manner in which the probe senses the sample surface, meaning when the probe scans the nanocoax structure and approaches the protruding outer electrode; it retracts to maintain constant sample-probe distance. Consequently, the measured intensity profile is somewhat distorted by this movement in both lateral scan directions resulting in a circular shape intensity. In the case where the excitation wavelength was 850 nm, on the other hand, the measured profiles are crescent-shaped and proximate to the coax core. This is similar to the calculated field because, in this case, the field is tightly confined to the surface of the coax core, which the NSOM probe can access without manifestation of the aforementioned artifact.

On the other hand, it is advantageous to know which order modes can be supported by the nanocoax structure and which were observed in the NSOM images, in order to know the mode dispersion as well as the propagation lengths. We used modal analysis on the same module of COMSOL for this purpose. In this context, it is well known that a coaxial waveguide supports a TEM (transverse electromagnetic) mode that does not present a cutoff wavelength, resulting in a long propagation length compared with the transverse dimensions of the waveguide. The supported higher modes are the $TE_{\lambda m}$ (transverse electric) and $TM_{\lambda m}$ (transverse magnetic), where the index λ determines the number of full periods of sinusoidal variation of the radial component of the *E*-field along any circle concentric to the inner electrode, and *m* denotes the number of half periods of sinusoidal variation in the azimuthal component of the *E*-field along the radial direction [29]. A third index *p* can be used to define the number of half periods of sinusoidal variation in the radial component of the *E*-field along the axial length *L* of the coaxial structure [29]. It is important to note that the TEM mode is excited mainly by a circularly polarized excitation field, while the TE modes stem from a linearly polarized field [6]. In our experimental conditions, discussed above, we used linearly polarized light, such that TE modes can be most readily excited. We also point out that if the excitation field is in the visible or infrared spectrum and the inner electrode is made with a noble metal (Ag, Au), TE modes can have plasmonic and/or photonic origin, depending on the order mode. That is, the lower order modes are plasmonic (near-infrared wavelength), while the higher order modes are photonic (visible wavelengths) [5].

We found that the supported modes in the nanocoax waveguide are $TE_{\lambda 1}$, with λ = 1, 2, 3, 4 and TM_{11}. We will retain the usual notation used in the coaxial modes to avoid confusion in our analysis, but one must keep in mind that some modes have plasmonic origin. In order to identify the plasmonic and photonic modes, we calculated the effective wavenumber of each mode by, $k_z' = n_{eff}' k_o$ where n_{eff}' is the real part of the effective refractive index. As shown in Fig. 3(a), it is clear that the TE_{11} and TE_{21} modes have plasmonic character while the TE_{31}, TE_{41} and TM_{11} modes are photonic, *i.e.* they lie above the light line. Even though the TEM mode cannot be excited in our experimental conditions, we calculated it and appears as a black line in Fig. 3(a). It is important to note that its behavior is plasmonic with no restriction in wavelength, a result previously reported [12].

Next, we calculated the propagation length *x* in the nanocoax via $x = k_z'' / 2$ where $k_z'' = n_{eff}'' k_o$, with n_{eff}'' the imaginary part of the effective refractive index of each mode [30]. Our results are shown in Fig. 3(b). Along the length *L* of the studied structure (shaded zone), the TE_{11}, TE_{21} and TE_{31} modes can reach the output of the nanocoax waveguide and

#210870 - $15.00 USD Received 25 Apr 2014; revised 19 May 2014; accepted 22 May 2014; published 2 Jun 2014

couple to the far field. On the other hand, the TE_{41} and TM_{11} modes have propagation lengths shorter than 1 μm and cannot be transmitted to the far field. This is likely due to the noble metals electrodes being lossy in the blue region of the visible spectrum. In Table 1 we present the maximum propagation length of each mode at the wavelength where it occurred. As expected, the propagation length decays strongly when the excitation wavelength approaches to the cutoff wavelength because the specific modes become evanescent. In Fig. 3(b), such values are nonzero because of the finite number of frequency steps used in our calculations.

Table 1. Maximum propagation length for each studied mode

	Mode					
	TEM	TE_{11}	TE_{21}	TE_{31}	TE_{41}	TM_{11}
Maximum propagation length (μm)	∞	9.27 μm @1.28 μm	5.61 μm @0.84 μm	3.43 μm @0.69 μm	0.96 μm @0.58 μm	0.81 μm @0.6 μm

Finally, in order to complete the optical characterization of the nanocoax array, we measured experimentally the transmittance of the sample as a function of the excitation wavelength using a fiber optic spectrometer (Ocean Optics 2000) attached to an optical microscope (Leica 6000M) at the image plane. The illumination sources were the same as the NSOM experiment, plus a broad spectrum white light emitting diode (LED). The experimental transmittance was defined as the ratio between the output intensity (after background subtraction) and the input intensity in percentage units, i.e., $T = 100\ (I_{out} - I_{bkg})/I_{in}$, where I_{out} is the transmitted intensity, I_{bkg} the background intensity and I_{in} the intensity in the absence of sample, *i.e.* the emission spectrum of the source. Figure 4 shows the experimentally-measured transmittance with white LED source (black line) and monochromatic sources (green figures), along with the calculated transmittance (red line). The later was obtained by using the same model as for the calculation of propagating fields inside the nanocoax.

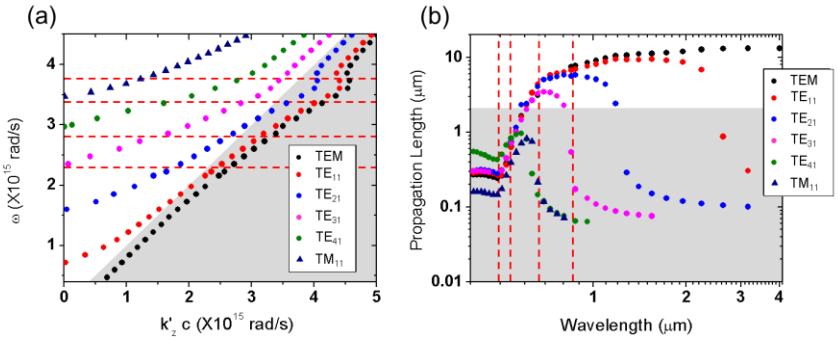

Fig. 3. (a) Calculated dispersion relations of the modes propagating in the nanocoax structure. The dashed lines represent the frequencies employed (excitation wavelengths) and the shaded zone represents the zone where plasmonic modes appear (i.e. separated from photonic modes by the light line ω = kc). (b) Calculated propagation lengths for the studied modes. The dashed lines represent the wavelengths used and the shaded zone indicates the length *L* of the nanocoax structure. Note the logarithmic scales.

It is clear that the transmittance is dominated by several peaks, at 761 nm and 874 nm in the calculated result and 591 nm and 647 nm in both measured and calculated results. These peaks can be explained as follows: in the coaxial structure, the propagating modes appear in three dimensions, *i.e.* radial, azimuthal and longitudinal. In this way, if the coaxial structure is long enough to support Fabry-Perot resonant cavity modes, the longitudinal order mode, according to phase-matching conditions in the coaxial structure, is $2k_z'L = 2p\pi - \phi_r$, with k_z'

#210870 - $15.00 USD Received 25 Apr 2014; revised 19 May 2014; accepted 22 May 2014; published 2 Jun 2014

for each specific mode inside the coaxial cavity. Here, L is the length of the coaxial structure, p the order of the resonant mode and ϕ_r a phase shift acquired in reflections of the mode at the cavity output [31]. If ϕ_r is small enough, the resonant condition becomes $k_z' L = p\pi$. Using the length of the nanocoax structure (L), each resonant order mode was calculated. Thus, as indicated in Fig. 4, the peak at 647 nm is due to a superposition of resonant longitudinal modes with orders p = 7 and 6 of the TE_{11} and TE_{21} modes, respectively, while at 591 nm the superposition is by orders 6 and 8 of the TE_{11} and TE_{31} modes, respectively. In both cases, such superposition of modes is the reason for the strong far field transmission reported in the experimental data. The coefficients of the modes superposition were not calculated in the present work. The peaks that appear in the calculated transmittance at 761 nm and 874 nm are related to the same process and due to order p = 3 of TE_{31} and TE_{21} modes, respectively. It is important to note that the weak transmittance at wavelengths shorter than 550 nm is due to the short propagation length of all the modes, since the plasma resonance wavelength occurs around such a wavelength, resulting in highly attenuated modes, Fig. 3(b).

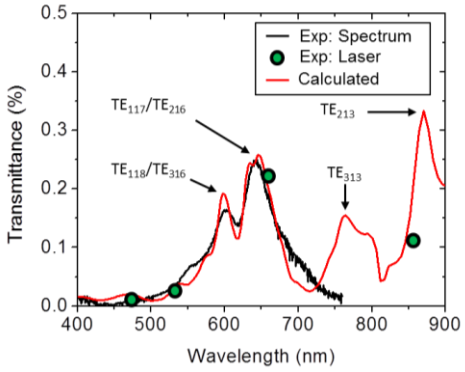

Fig. 4. Experimental (black line and green circles) and calculated (red line) transmission. Circles were obtained using single wavelength sources. The resonant modes discussed in the text are indicated.

4. Conclusions

In summary, experimental observations of plasmonic and photonic modes propagating in nanocoax structures are presented for the first time, using near-field microscopy. Comparison between NSOM experiments and calculations demonstrate that the experimental data are related to the propagating electromagnetic field in the nanocoax structure. By calculating $\boldsymbol{k}_z$ of each mode, we determined the propagation lengths and conclude that the TE_{11}, TE_{21} and TE_{31} modes can propagate along the full nanocoax length and couple to the far field, in the spectral range analyzed experimentally. These results are relevant to understanding the physics of propagated fields in nanocoax structures and their potential applications in the subwavelength nanoscale manipulation of light including, for example, polarization-preserving optical waveguides for optical communication.

Acknowledgments

This work was supported by the W. M. Keck Foundation. J.M.M. acknowledges support from CONACyT, fellowship number 203768.

#210870 - $15.00 USD Received 25 Apr 2014; revised 19 May 2014; accepted 22 May 2014; published 2 Jun 2014